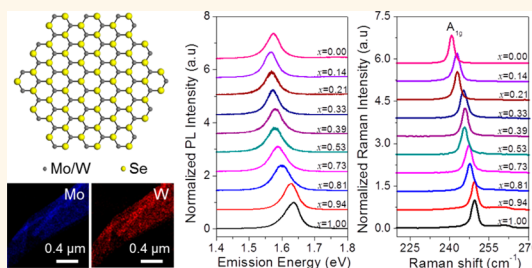


Two-Dimensional Molybdenum Tungsten Diselenide Alloys: Photoluminescence, Raman Scattering, and Electrical Transport

Mei Zhang,^{†,⊗} Juanxia Wu,^{‡,§,⊗} Yiming Zhu,^{†,⊗} Dumitru O. Dumcenco,^{||,△} Jinhua Hong,[⊥] Nannan Mao,^{†,‡} Shibin Deng,[‡] Yanfeng Chen,[†] Yanlian Yang,[†] Chuanhong Jin,[⊥] Sunil H. Chaki,[#] Ying-Sheng Huang,^{||,*} Jin Zhang,^{‡,*} and Liming Xie^{†,*}

[†]CAS Key Laboratory of Standardization and Measurement for Nanotechnology, National Center for Nanoscience and Technology, Beijing 100190, People's Republic of China, [‡]Center for Nanochemistry, Beijing National Laboratory for Molecular Sciences, Key Laboratory for the Physics and Chemistry of Nanodevices, State Key Laboratory for Structural Chemistry of Unstable and Stable Species, College of Chemistry and Molecular Engineering, Peking University, Beijing 100871, People's Republic of China, [§]Academy for Advanced Interdisciplinary Studies, Peking University, Beijing 100871, People's Republic of China, ^{||}Department of Electronic Engineering, National Taiwan University of Science and Technology, Taipei 106, Taiwan Republic of China, [⊥]State Key Laboratory of Silicon Materials, Key Laboratory of Advanced Materials and Applications for Batteries of Zhejiang Province and Department of Materials Science and Engineering, Zhejiang University, Hangzhou 310027, People's Republic of China, and [#]P. G. Department of Physics, Sardar Patel University, Vallabh Vidyanagar, Gujarat 388120, India. [⊗]M. Zhang, J. Wu, and Y. Zhu contributed equally. [△]Present address: Electrical Engineering Institute, Ecole Polytechnique Federale de Lausanne (EPFL), CH-1015 Lausanne, Switzerland.

ABSTRACT Two-dimensional transition-metal dichalcogenide alloys have attracted intense attention due to their tunable band gaps. In the present work, photoluminescence, Raman scattering, and electrical transport properties of monolayer and few-layer molybdenum tungsten diselenide alloys ($\text{Mo}_{1-x}\text{W}_x\text{Se}_2$, $0 \leq x \leq 1$) are systematically investigated. The strong photoluminescence emissions from $\text{Mo}_{1-x}\text{W}_x\text{Se}_2$ monolayers indicate composition-tunable direct band gaps (from 1.56 to 1.65 eV), while weak and broad emissions from the bilayers indicate indirect band gaps. The first-order Raman modes are assigned by polarized Raman spectroscopy. Second-order Raman modes are assigned according to its frequencies. As composition changes in $\text{Mo}_{1-x}\text{W}_x\text{Se}_2$ monolayers and few layers, the out-of-plane A_{1g} mode showed one-mode behavior, while B_{2g}^{-1} (only observed in few layers), in-plane E_{2g}^{-1} , and all observed second-order Raman modes showed two-mode behaviors. Electrical transport measurement revealed n-type semiconducting transport behavior with a high on/off ratio ($>10^5$) for $\text{Mo}_{1-x}\text{W}_x\text{Se}_2$ monolayers.



KEYWORDS: transition-metal dichalcogenide · semiconductor alloy · tunable band gap · photoluminescence · Raman effect · electrical property

Two-dimensional (2D) semiconductors, such as transition-metal dichalcogenide (TMD) monolayers, have attracted intense interest because of their direct band gaps.^{1–5} MoSe_2 and WSe_2 monolayers are two important 2D semiconductors toward light harvesting because of their suitable band gaps (1.44 and 1.54 eV from calculation^{6,7}) for solar cells. Thin-film solar cells based on graphene/ MoSe_2 , graphene/ WSe_2 heterojunctions have been demonstrated recently, showing a maximum internal efficiency up to 30% with plasmonic enhancing.⁸ Simulation also shows that graphene/ MoSe_2 and graphene/ WSe_2 heterojunctions can achieve a power conversion efficiency

up to 1% for these ultrathin solar cells and hence have an ultrahigh power/mass ratio (2500 W/kg, more than 1000 times higher than silicon thin-film solar cells).⁹ 2D transition-metal dichalcogenide alloys can have tunable band gaps and CB/VB positions^{10–12} and then can be used to fine-tune the optical absorption and fine align the energy levels in these heterostructures for higher performance.^{13,14} Here we have mechanically exfoliated $\text{Mo}_{1-x}\text{W}_x\text{Se}_2$ monolayers and few layers. STEM-EDS showed a homogeneous distribution of different elements in the alloys. Photoluminescence characterization showed composition-dependent direct band gap emissions from 1.56 to 1.65 eV for

* Address correspondence to
xielm@nanoctr.cn;
jinzhang@pku.edu.cn;
ysh@mail.ntust.edu.tw.

Received for review April 13, 2014
and accepted June 2, 2014.

Published online June 02, 2014
10.1021/nn5020566

© 2014 American Chemical Society

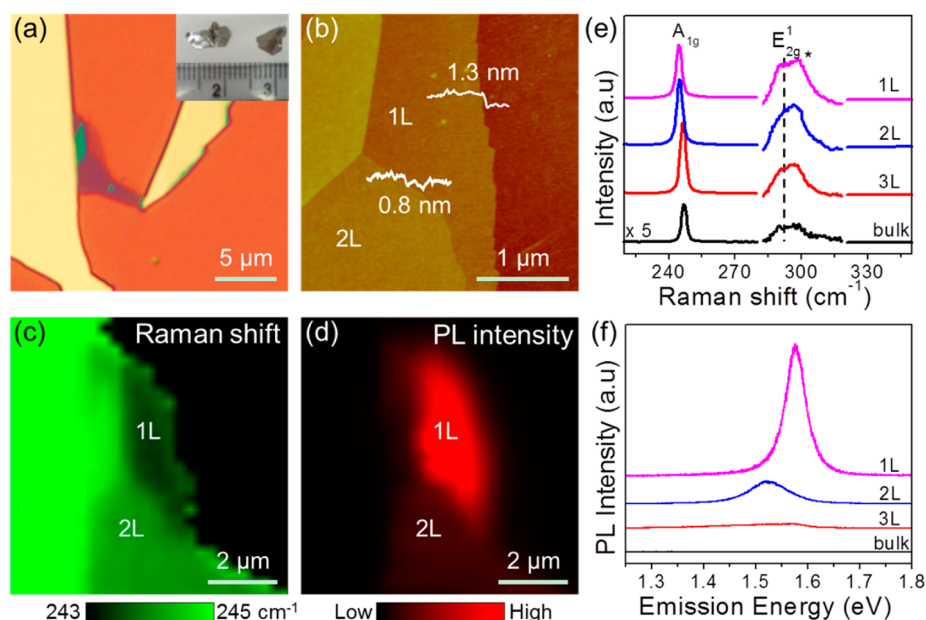


Figure 1. (a) Optical and (b) AFM image of $\text{Mo}_{0.67}\text{W}_{0.33}\text{Se}_2$ sheets. Inset in panel (a) is a photograph of $\text{Mo}_{0.67}\text{W}_{0.33}\text{Se}_2$ single crystals. Mapping images of (c) A_{1g} frequency and (d) PL intensity of the same $\text{Mo}_{0.67}\text{W}_{0.33}\text{Se}_2$ sheets. (e) Raman and (f) PL spectra of $\text{Mo}_{0.67}\text{W}_{0.33}\text{Se}_2$ monolayer (1L, magenta lines), bilayer (2L, blue lines), trilayer (3L, red lines), and bulk samples (black lines). The excitation laser wavelength was 514.5 nm. The Raman peak labeled by * was from the SiO_2/Si substrate.

monolayers. Raman spectroscopic characterization showed one-mode behavior for the A_{1g} mode and two-mode behaviors for first-order modes E_{2g}^1 and B_{2g}^1 and the observed second-order Raman modes. Field-effect transistors fabricated on monolayers showed n-type transport with high on/off ratios ($>10^5$).

RESULTS AND DISCUSSION

$\text{Mo}_{1-x}\text{W}_x\text{Se}_2$ monolayers consist of two Se atomic layers and a sandwiched metal (Mo, W) atom layer.^{15,16} Figure 1a shows an optical image of exfoliated $\text{Mo}_{0.67}\text{W}_{0.33}\text{Se}_2$ ($x = 0.33$) flakes with monolayer and bilayer regions. The red channel contrasts of the monolayer and bilayer regions are $\sim 10\%$ and $\sim 20\%$, respectively.¹⁷ The inset in Figure 1a is a photograph of $\text{Mo}_{0.67}\text{W}_{0.33}\text{Se}_2$ single crystals. The atomic force microscopy (AFM) image of this alloy sheet is shown in Figure 1b, showing a height of about 1.3 nm for the monolayer, which is larger than the theoretical interlayer distance in $\text{Mo}_{0.67}\text{W}_{0.33}\text{Se}_2$ bulk materials (~ 0.6 nm). This phenomenon is due to the instrumental offset (~ 0.5 nm)^{18,19} and is commonly observed in AFM imaging of transition-metal dichalcogenide monolayers^{20–22}

For $\text{Mo}_{0.67}\text{W}_{0.33}\text{Se}_2$ alloy sheets, the PL image shows that emission from monolayers is stronger than that from bilayers, while there is much weaker emission from the thicker and bulk materials (Figure 1d,f), suggesting transition from indirect band gap to direct band gap when $\text{Mo}_{0.67}\text{W}_{0.33}\text{Se}_2$ thinned from bulk to monolayer.^{12,23} From monolayer to bulk $\text{Mo}_{0.67}\text{W}_{0.33}\text{Se}_2$ alloys, the first-order Raman peak A_{1g} mode is stiffened from 243.4 to 245.6 cm^{-1} , while the E_{2g}^1 mode is slightly softened from 288.5 to 287.7 cm^{-1} (Figure 1c,e). The

assignment of the E_{2g}^1 mode is confirmed by polarized Raman spectroscopy (Figure S2). Note that the correct Raman notation should be A_1' and E' for odd layers, and A_{1g} and E_g for even layers.^{24,25} Here for simplicity, the notations of Raman modes A_{1g} and E_{2g}^1 (correct for bulk materials) are used for $\text{Mo}_{1-x}\text{W}_x\text{Se}_2$ monolayers and few layers in this article. Similar to that in MoSe_2 and WSe_2 , the A_{1g} mode shifted to higher frequency with increasing sample thickness. Raman frequency variation within the monolayer and bilayer region is less than 0.3 cm^{-1} , indicating homogeneous composition in the micrometer scale. Raman and PL spectra of $\text{Mo}_{1-x}\text{W}_x\text{Se}_2$ with other W compositions (Figures S7–S16) showed similar characteristics to that in $\text{Mo}_{0.67}\text{W}_{0.33}\text{Se}_2$, i.e., much stronger PL emission from monolayers, and stiffening of A_{1g} and slight softening of E_{2g}^1 as the layer number increases.

Further high-angle annular dark field (HAADF) scanning transmission electron microscopy (STEM) with EDS capability was used for mapping element distributions in nanometer scales. Figure 2a shows a STEM-HAADF image of as-grown $\text{Mo}_{0.47}\text{W}_{0.53}\text{Se}_2$ few layers. The inset in Figure 2a is an atomically resolved image to reveal its honeycomb atom arrangement. Figure 2b shows the EDS spectrum of the $\text{Mo}_{0.47}\text{W}_{0.53}\text{Se}_2$ sheet with well-resolved Mo, W, and Se peaks. The EDS mapping (Figure 2c–e) revealed a uniform distribution of Mo, W, and Se in the sample.

PL measurements on $\text{Mo}_{1-x}\text{W}_x\text{Se}_2$ monolayers with different W compositions showed tunable band gap exciton emissions (Figure 3a). As W composition x increases, the PL emission shows a bowing effect, in which emission energy first red shifts to a minimum value at around $x = 0.2$ – 0.3 and then monotonically

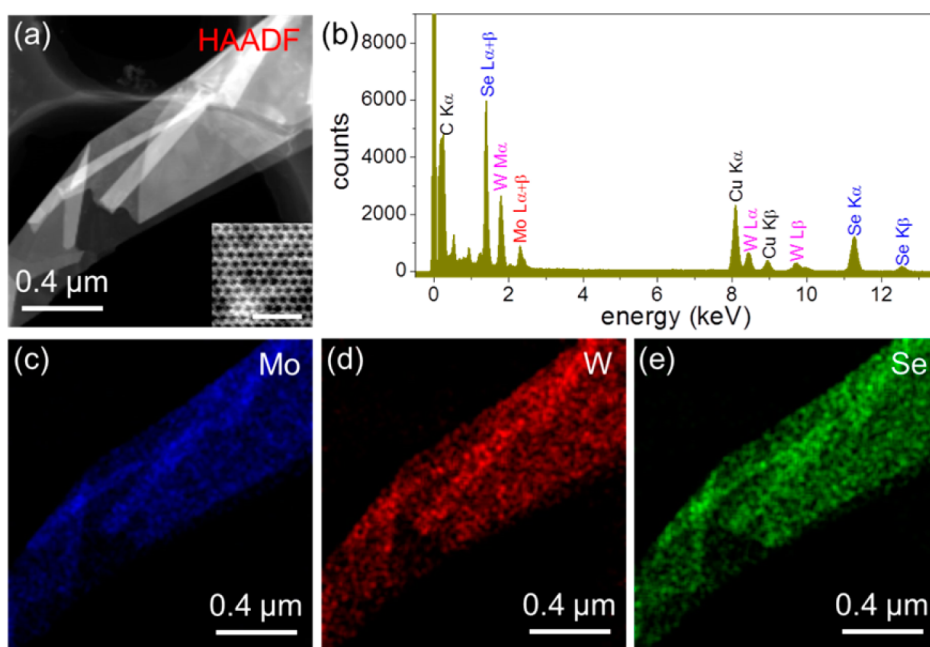


Figure 2. (a) HAADF STEM image and (b) EDS spectrum of $\text{Mo}_{0.47}\text{W}_{0.53}\text{Se}_2$ flakes. Inset in (a) is a high-resolution STEM image, and the scale bar is 3 nm. (c) Mo, (d) W, and (e) Se element mapping image for the same sheet.

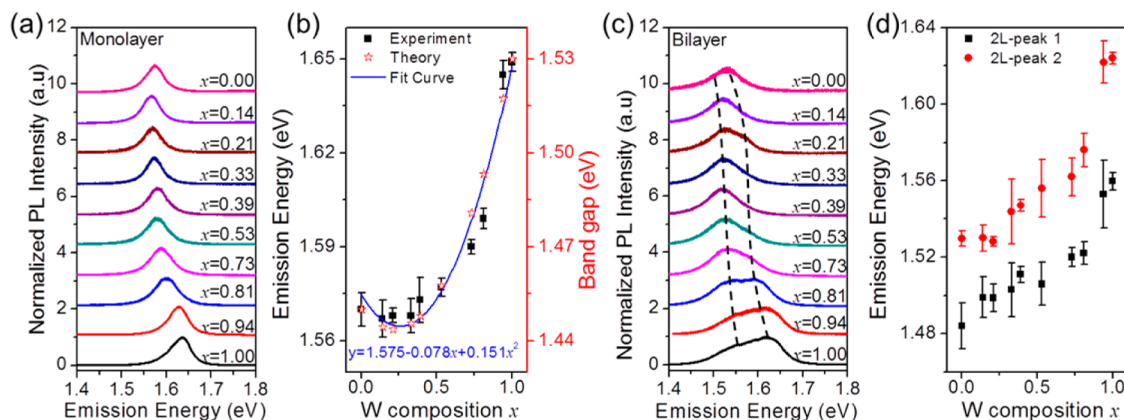


Figure 3. Composition-dependent (a) PL spectra and (b) PL emission energies of $\text{Mo}_{1-x}\text{W}_x\text{Se}_2$ monolayer alloys. The blue line in (b) is the parabola fitting for the experimental emission energy. Composition-dependent (c) PL spectra and (d) PL emission energies of $\text{Mo}_{1-x}\text{W}_x\text{Se}_2$ bilayers. The black dashed lines in (c) show the emission energy shift of the two peaks. The excitation laser wavelength was 514.5 nm.

blue shifts.²⁶ This result can be attributed to the linearity of VB and deviation from linearity of the CB energy variation with the W composition.²⁷ Therefore, the band gap emission of the $\text{Mo}_{1-x}\text{W}_x\text{Se}_2$ monolayers can be continuously tuned from 1.56 eV (reached at $x = 0.21$) to 1.65 eV (reached at $x = 1$). The PL emission bowing in $\text{Mo}_{1-x}\text{W}_x\text{Se}_2$ monolayer alloys can be described by the following function:^{26,27}

$$E_{\text{PL}, \text{Mo}_{1-x}\text{W}_x\text{Se}_2} = xE_{\text{PL}, \text{WSe}_2} + (1-x)E_{\text{PL}, \text{MoSe}_2} - bx(1-x) \quad (1)$$

where b is the bowing parameter. Fitting the experimental results with eq 1 gives a bowing parameter of 0.151 eV (Figure 3b), which is well consistent with the calculated results ($b = 0.14$ eV).²⁷

For bilayer MoSe_2 and WSe_2 , the energy difference between the indirect and direct transitions is small (~ 20 meV), and then both emissions can be observed in experiments.^{28,29} The PL spectra of $\text{Mo}_{1-x}\text{W}_x\text{Se}_2$ bilayers with different W composition also shows multiple components, which can be assigned to direct and indirect band gap exciton emissions (Figure 3c). The emission peak position versus W composition is presented in Figure 3d. Further theoretical simulation is needed to elucidate the observed composition-dependent behaviors in $\text{Mo}_{1-x}\text{W}_x\text{Se}_2$ bilayers.

To further confirm the assignment of Raman modes in $\text{Mo}_{1-x}\text{W}_x\text{Se}_2$ alloys, polarized Raman spectroscopy was carried out. For monolayer MoSe_2 , the A_{1g} and E_{2g}^1 modes are centered at 240.1 and 287.1 cm^{-1} ,

respectively.^{1,30,31} However, for the WSe₂ monolayer, there are conflicting reports on the assignment of A_{1g} and E_{2g}¹ modes. Theoretical studies have suggested that A_{1g} and E_{2g}¹ are degenerate at ~250 cm⁻¹ in the few-layer WSe₂,^{32,33} while several experimental studies have assigned the Raman peaks at 249.6 and 260.8 cm⁻¹ to E_{2g}¹ and A_{1g} phonon modes,^{28,29,34} respectively. In our work, monolayer WSe₂ (Figure S4a) exhibits a prominent Raman mode at ~249.6 cm⁻¹ and a weak peak at ~261.2 cm⁻¹ under both parallel (Z(XX)Z̄) and cross (Z(YX)Z̄) polarization conditions with 514.5 nm excitation. This indicates that the 261 cm⁻¹ peak should not be A_{1g} mode. When the thickness increases from monolayer to bulk, the 249.6 cm⁻¹ peak (Figure S4a) splits into two peaks at ~248.0 and 251.2 cm⁻¹ (Figure S 4d), in which the 251.2 cm⁻¹ peak is active only under parallel polarization configuration, and the 248.0 cm⁻¹ peak is active at both parallel and cross-polarization configurations. These results suggest that the 251.2 cm⁻¹ peak should be A_{1g} mode and the 248.5 cm⁻¹ peak should be E_{2g}¹ mode. A similar thickness and polarization dependence of the phonon modes are observed for WSe₂ when the incident laser wavelength is 632.8 nm (Figure S4e–h). Therefore, for monolayers, the 249.6 cm⁻¹ peak can be assigned to the A_{1g} and E_{2g}¹ modes, and the 261.2 cm⁻¹ peak can be assigned to a second-order Raman peak.

When TMDs are thinned from 3D crystals to 2D crystals,²⁵ some Raman inactive modes in the bulk may become Raman active in the few layers because of the reduced symmetry [from D_{6h} to D_{3h} (odd layers) or D_{3d} (even layers)].^{35,36} Theoretical studies have predicted that the out-of-plane vibrational mode B_{2g}¹ (correct notation is A₁'² for odd layers and A_{1g}² for even layers), which is Raman inactive in bulk WSe₂ and MoSe₂, becomes Raman active when the thickness thins to a few layers due to the break of the symmetry selection rules in the resonant scattering processes.³⁵ The polarized and unpolarized Raman spectra of MoSe₂ and WSe₂ with different thicknesses are shown in Figure 4 and Figures S7, S16. The B_{2g}¹ mode, which lies around 353 and 309 cm⁻¹ for MoSe₂ and WSe₂, respectively, can be detected only under parallel polarization in few layers. This Raman peak slightly shifts to lower frequency as the layer number increases, which can be attributed to the surface effects.³⁵ Additionally, the E_{1g} mode (corresponding notations are E_g'² and E_g² for odd layers and even layers, respectively), which results from the opposite moving of the two Se atoms parallel to the layer planes,³⁶ was observed in few-layer MoSe₂ (Figures 4 and S16) under both parallel and cross-polarization configurations. Note, the notations of Raman modes in bulk materials are used for Mo_{1-x}W_xSe₂ monolayers and few layers in this article for simplicity.

The frequencies of second- and higher-order Raman modes should be equal to the sum of frequencies of

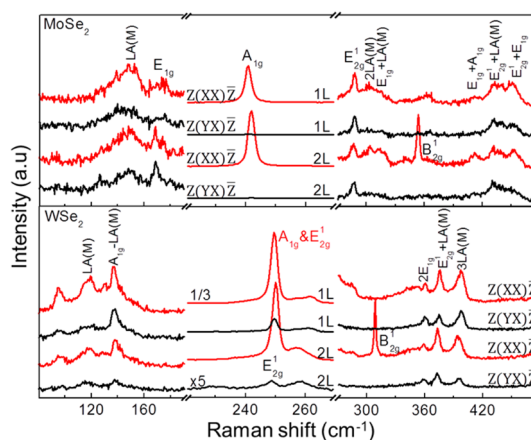


Figure 4. Polarized Raman spectra of MoSe₂ (top) and WSe₂ (bottom) monolayers and bilayers in the range 80–480 cm⁻¹ under parallel (Z(XX)Z̄, red lines) and cross (Z(YX)Z̄, black lines) polarization configurations. Assignment of the first- and second-order Raman modes is marked at the top of the spectra. For clarity, the spectra in the range 220–270 cm⁻¹ are multiplied by a factor in magnitude labeled on the corresponding spectra. The excitation laser wavelength was 514.5 nm.

the involved phonon modes.^{37–40} According to the above rules, the assignment of the relatively weak second- and higher-order Raman peaks in MoSe₂ and WSe₂ has been carried out (Figure 4). The second-order Raman peaks also showed polarization-dependent intensity. For few-layer MoSe₂, the overtone mode 2LA(M) and combination mode E_{1g} + A_{1g} can be observed only in the parallel polarization configuration, while other combination modes can be detected under both parallel and cross-polarization configurations. However, the combination modes of few-layer WSe₂ showed different intensities on different polarization configurations.

Figure 5a,b show unpolarized Raman spectra of Mo_{1-x}W_xSe₂ monolayers with different W composition *x* and the corresponding composition-dependent Raman frequencies. Similar to that of Mo_{1-x}W_xSe₂ alloys,^{41,42} the out-of-plane A_{1g} and in-plane E_{2g}¹ modes show one-mode and two-mode behaviors, respectively. The A_{1g} mode continuously shifts from 240.1 to 249.3 cm⁻¹ when the W composition *x* increases from 0 to 1, which is close to a linear dependence on the W composition. As shown in Figure 5a, the MoSe₂-like E_{2g}¹ shifts to lower frequency as the W composition increases. In addition, the second-order Raman peaks also shift and showed two-mode behaviors as the W composition changes; that is, there are two branches of E_{2g}¹ + LA(M) mode: one branch is related to MoSe₂ (at ~432.7 cm⁻¹ in MoSe₂) and the other branch is related to WSe₂ (at ~373.6 cm⁻¹ in WSe₂). When the W composition *x* increases, all MoSe₂-like second-order Raman peaks slightly shift to lower frequencies. WSe₂-like Raman peaks showed different shift directions: WSe₂-like A_{1g}-LA(M) and 2E_{1g} modes upshift, 3LA(M) downshifts, and E_{2g}¹ + LA(M) has almost no shift.

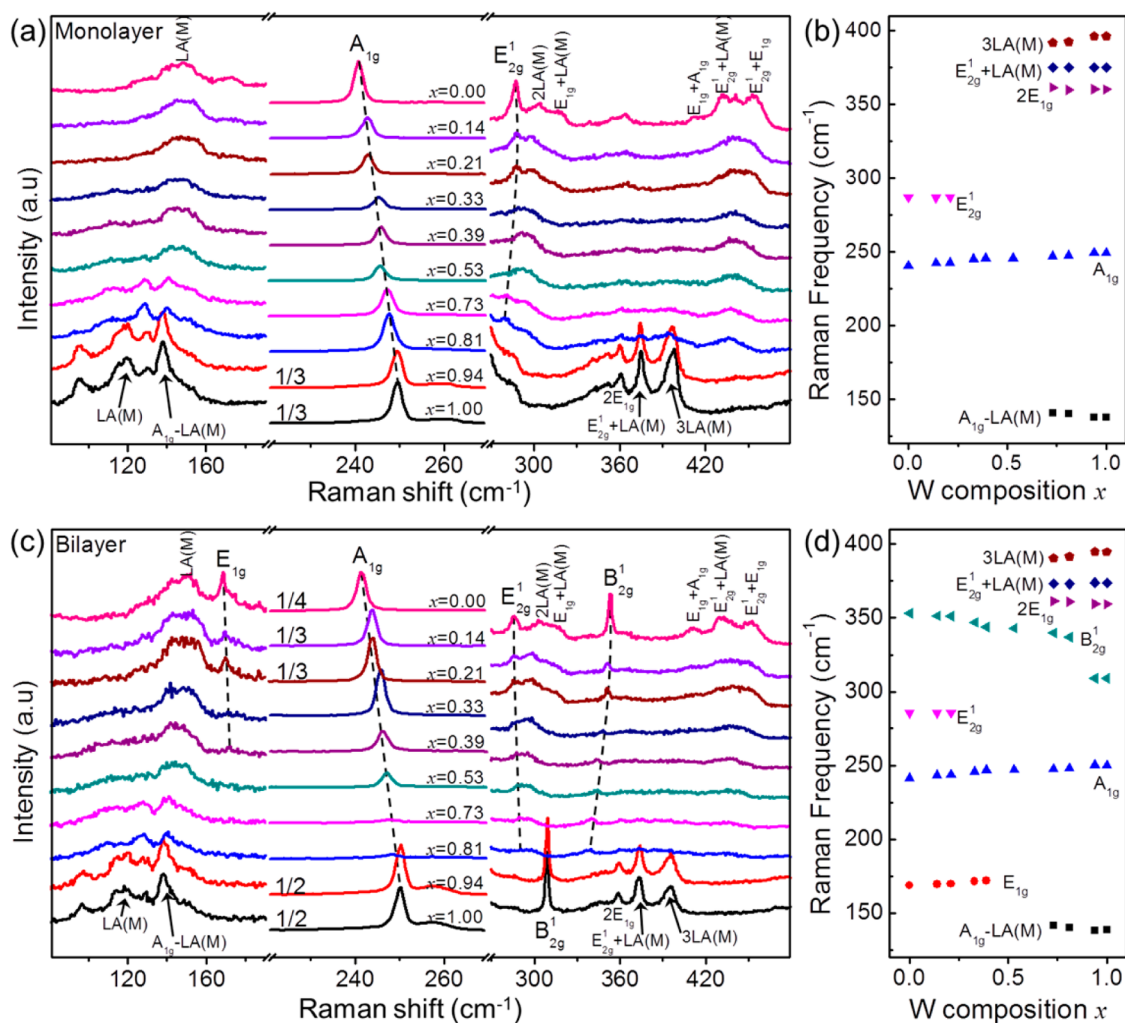


Figure 5. (a) Raman spectra of $\text{Mo}_{1-x}\text{W}_x\text{Se}_2$ monolayers with different W composition x in the range $80\text{--}480\text{ cm}^{-1}$. (b) Composition-dependent Raman frequencies of $\text{Mo}_{1-x}\text{W}_x\text{Se}_2$ monolayer alloys. (c) Raman spectra of $\text{Mo}_{1-x}\text{W}_x\text{Se}_2$ bilayers with different W composition x . (d) Composition-dependent Raman frequencies of $\text{Mo}_{1-x}\text{W}_x\text{Se}_2$ bilayer alloys. All the spectra are calibrated with the 520 cm^{-1} Raman peak from the Si substrate. The black dashed lines in (a) and (c), guides for the eye, show the frequency shift of the first-order Raman modes with different W compositions x . For clarity, the intensity of spectra in the range $220\text{--}270\text{ cm}^{-1}$ is magnified by a factor labeled on the corresponding spectra. The excitation laser wavelength was 514.5 nm .

Raman spectra and Raman frequency shift of $\text{Mo}_{1-x}\text{W}_x\text{Se}_2$ bilayers with different W composition are shown in Figure 5c,d. Similar to that in monolayers, the A_{1g} mode shows one-mode behavior, while other modes show two-mode behaviors. When the W composition increases, the E_{1g} mode of MoSe_2 slightly shifts to higher frequency, while the MoSe_2 -like B_{2g}^1 shifts to lower frequency. The MoSe_2 -like B_{2g}^1 mode can be observed for x in the range $0\text{--}0.81$, while the WSe_2 -like B_{2g}^1 mode can be observed only for the last two composition alloys ($x = 0.94$ and 1.00).

In addition, the modified random element isodisplacement (MREI) model,⁴¹ which is based on the assumption of isodisplacement of the same atoms and the randomness distribution of Mo/W atoms, can be used to fit the composition-dependent Raman frequencies of the A_{1g} mode for $\text{Mo}_{1-x}\text{W}_x\text{Se}_2$ monolayers and bilayers (Figure S6). The composition-dependent A_{1g} frequency,

analyzed using the MREI model, can be expressed as

$$\omega_{A_{1g}} = \left[\frac{(1-x)F_1 + xF_2}{m_{\text{Se}}} \right]^{1/2} = \left[\frac{(1-x)(1-\theta x)F_{10} + x(1-\theta x)F_{20}}{m_{\text{Se}}} \right]^{1/2} \quad (2)$$

where m_{Se} is the atomic mass of Se; F_1 and F_2 are the force constants of Mo–Se and W–Se interactions, respectively; F_{10} and F_{20} are limiting values of F_1 and F_2 as x is reduced to 0; and θ is a parameter that is associated with the variation of force constant in the alloys. The fitting result gives a more accurate composition-dependent frequency shift of the A_{1g} mode,

$$\omega_{A_{1g}}^{1\text{L}} = 240.1(1 + 0.057x - 0.023x^2) \quad (3)$$

$$\omega_{A_{1g}}^{2\text{L}} = 241.0(1 + 0.052x - 0.018x^2) \quad (4)$$

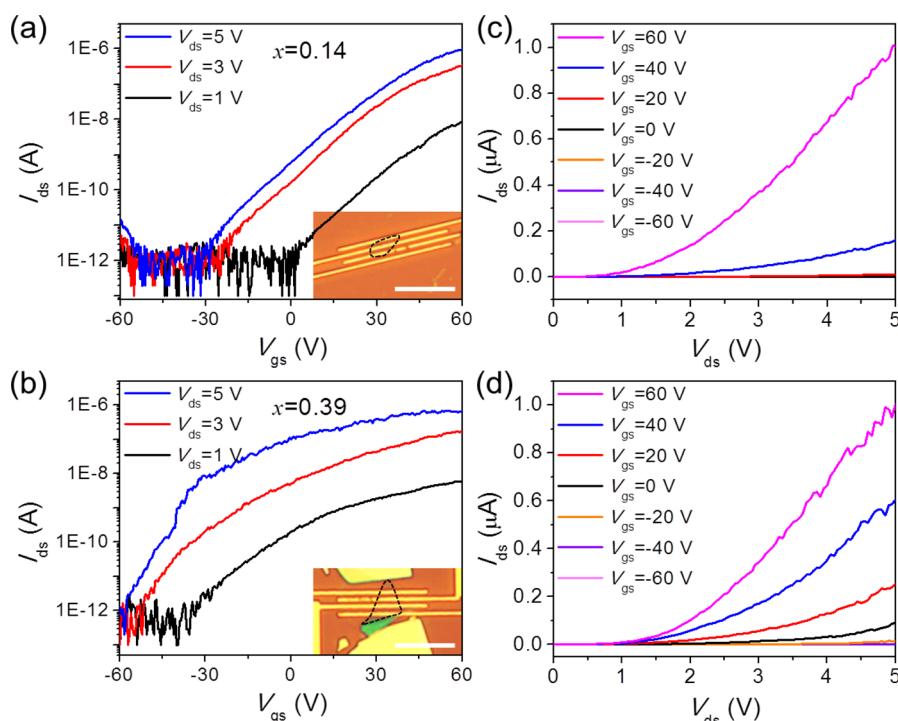


Figure 6. (a, b) Transfer curves (I_{ds} – V_{gs}) under different source–drain voltage and (c, d) output curves (I_{ds} – V_{ds}) under different bottom gate voltage of $\text{Mo}_{1-x}\text{W}_x\text{Se}_2$ monolayer FETs for (a, c) $x = 0.14$ and (b, d) $x = 0.39$. Insets in (a) and (b) are the optical images of the devices, and the scale bar in the insets is $10\ \mu\text{m}$. The black dashed lines in the insets are the profiles of the monolayer samples.

which can be used to quantify the W composition for $\text{Mo}_{1-x}\text{W}_x\text{Se}_2$ with unknown composition.

Field effect transistors (FETs) were also fabricated on $\text{Mo}_{1-x}\text{W}_x\text{Se}_2$ monolayers. Figure 6 shows the typical transfer and output curves for $\text{Mo}_{1-x}\text{W}_x\text{Se}_2$ monolayers (more device data in Figure S17). All $\text{Mo}_{1-x}\text{W}_x\text{Se}_2$ monolayer FETs exhibited n-type semiconducting transport behavior with high on–off ratios ($>10^5$). The field effect carrier mobility of $\text{Mo}_{1-x}\text{W}_x\text{Se}_2$ monolayer devices can be calculated from the transfer curves based on the following equation:^{43,44}

$$\mu_{\text{FE}} = \frac{dI_{ds}}{dV_{gs}} \frac{L}{W} \frac{1}{C_g V_{ds}} \quad (5)$$

where L and W are channel length and width of the device, respectively; C_g is the gate capacitance of the dielectric layer; I_{ds} is the drain–source current; and V_{gs} is the gate voltage. dI_{ds}/dV_{gs} can be calculated from the slope of the transfer curves. The calculated mobility of $\text{Mo}_{1-x}\text{W}_x\text{Se}_2$ monolayer FETs with $x = 0.14, 0.33, 0.39$, and 1.00 was about $0.215, 0.129, 7.8 \times 10^{-2}$, and $2.97 \times 10^{-3}\ \text{cm}^2\text{V}^{-1}\ \text{s}^{-1}$, respectively. The low mobility for the $\text{Mo}_{1-x}\text{W}_x\text{Se}_2$ monolayer FETs resulted from the poor contact between the electrode (Ti/Au) and the monolayers. The onset threshold gate voltage shifts to more

negative values at higher W compositions, indicating that the valence and conduction band shift as the W composition changes.

CONCLUSION

In conclusion, we have studied PL, Raman, and electrical properties on $\text{Mo}_{1-x}\text{W}_x\text{Se}_2$ ($0 \leq x \leq 1$) monolayers and few layers. The $\text{Mo}_{1-x}\text{W}_x\text{Se}_2$ monolayers exhibited strong PL emission, indicating the direct band gap nature, while the bilayers and few layers are indirect band gap semiconductors. Composition-dependent PL emission showed tunable band gaps for the $\text{Mo}_{1-x}\text{W}_x\text{Se}_2$ monolayer alloys (from ~ 1.56 to $\sim 1.65\ \text{eV}$). First- and second-order Raman modes were observed in the frequency range $80\text{--}480\ \text{cm}^{-1}$. The assignment of first-order Raman modes is confirmed using polarized Raman spectroscopy, and the second-order modes are assigned based on its frequencies. Composition-dependent Raman frequencies of the A_{1g} mode are fitted by the MREI model. Field effect transistors based on the monolayer alloys have shown n-type transport behavior with a high on/off ratio ($>10^5$). The composition- and layer-dependent properties of 2D $\text{Mo}_{1-x}\text{W}_x\text{Se}_2$ alloys make it promising for future nanoelectronics, optoelectronics, and solar cells.

EXPERIMENTAL SECTION

$\text{Mo}_{1-x}\text{W}_x\text{Se}_2$ single crystals were grown by the chemical vapor transport method. The W composition in $\text{Mo}_{1-x}\text{W}_x\text{Se}_2$

alloys was determined by energy-dispersive X-ray spectroscopy (EDX), which is shown in the Supporting Information (Figure S1).

Mo_{1-x}W_xSe₂ monolayer and few-layer alloy samples were prepared by micromechanical exfoliation of Mo_{1-x}W_xSe₂ single crystals on SiO₂/Si (300 nm thick oxide) substrates using Scotch tape. The monolayer and few-layer Mo_{1-x}W_xSe₂ samples were distinguished by a combination of optical microscopy (on an Olympus BX51 microscope) and atomic force microscopy (on a Veeco Dimension 3100 with tapping-mode).

PL and Raman spectra were collected on a JY Horiba HR800 Raman system with 632.8 and 514.5 nm lasers, a 100× objective (NA = 0.9, corresponding XY resolution of ~1 μm), and an 1800 lines/mm grating (corresponding a spectral resolution of ~0.6 cm⁻¹). The laser power was kept below 0.5 mW to avoid possible heating effect. In the polarization-dependent Raman experiments, the parallel polarization, *i.e.*, Z(XX)Z configuration, was measured by placing an analyzer between edge filter and detector, and the polarization direction of the scattered light was parallel to that of the incident laser. The cross-polarization, *i.e.*, (Z(YX)Z) configuration, was measured by placing a half-wave plate in the laser path and placing an analyzer between the edge filter and the detector in the signal path. PL and Raman mapping experiments were taken by using an XYZ microscope stage. The intensity and peak position of the PL and Raman peaks were obtained by fitting them with Gaussian and Lorentzian functions, respectively.

HAADF-STEM imaging and STEM-EDS mapping were conducted on an FEI Titan Chemi-STEM operated at 80 kV. This microscope was equipped with a Bruker Super-X EDS system with ultralarge windows and short working distance for X-ray detection. A typical probe current of 80 pA was used for the HAADF imaging and 200 pA for EDS mapping to obtain a high enough X-ray signal.

Field effect transistors based on the monolayer Mo_{1-x}W_xSe₂ alloys were fabricated by standard electron-beam lithography and thermal evaporation of 5 nm Ti and 50 nm Au. Electrical measurements were performed on an Agilent B1500A semiconductor device analyzer in a vacuum (Janis ST500 probe station, ~10⁻⁵ Torr).

Conflict of Interest: The authors declare no competing financial interest.

Acknowledgment. L.X. acknowledges support from NSFC (21373066 and 11304052) and China Postdoctoral Science Foundation (2013M540900). J.Z. acknowledges support from NSFC (21233001, 21129001, 51272006, and 51121091) and MOST (2011YQ0301240201 and 2011CB932601). Y.-S.H. acknowledges support from the National Science Council of Taiwan under Projects NSC 100-2112-M-011-001-MY3 and NSC 101-2811-M-011-002. C.J. acknowledges support from NFSC (51222202), the National Basic Research Program of China (2014CB932500), the Program for Innovative Research Team in University of Ministry of Education of China (IRT13037), and the Fundamental Research Funds for the Central Universities (2014XZZX003-07). The work on microscopy was mainly done at the Center of Electron Microscopy of Zhejiang University.

Supporting Information Available: EDX characterization results of Mo_{1-x}W_xSe₂ single crystals, schematics of atomic displacements of the first-order modes, polarized Raman spectra of WSe₂ with different layer numbers under 514.5 and 632.8 nm laser excitation, polarized Raman spectra of Mo_{0.17}W_{0.83}Se₂ and Mo_{0.79}W_{0.21}Se₂, composition-dependent A_{1g} frequency in monolayer and bilayer Mo_{1-x}W_xSe₂ alloys using the MREI model, and optical, AFM, PL emission, and Raman spectra of Mo_{1-x}W_xSe₂ with different W composition *x*. This material is available free of charge via the Internet at <http://pubs.acs.org>.

REFERENCES AND NOTES

- Ding, Y.; Wang, Y. L.; Ni, J.; Shi, L.; Shi, S. Q.; Tang, W. H. First Principles Study of Structural, Vibrational and Electronic Properties of Graphene-Like MX₂ (M=Mo, Nb, W, Ta; X=S, Se, Te) Monolayers. *Phys. B (Amsterdam, Neth.)* **2011**, *406*, 2254–2260.
- Li, H.; Lu, G.; Wang, Y. L.; Yin, Z. Y.; Cong, C. X.; He, Q. Y.; Wang, L.; Ding, F.; Yu, T.; Zhang, H. Mechanical Exfoliation

and Characterization of Single- and Few-Layer Nanosheets of WSe₂, TaS₂, and TaSe₂. *Small* **2013**, *9*, 1974–1981.

- Yin, Z. Y.; Li, H.; Li, H.; Jiang, L.; Shi, Y. M.; Sun, Y. H.; Lu, G.; Zhang, Q.; Chen, X. D.; Zhang, H. Single-Layer MoS₂ Phototransistors. *ACS Nano* **2012**, *6*, 74–80.
- Sun, L. F.; Yan, J. X.; Zhan, D.; Liu, L.; Hu, H. L.; Li, H.; Tay, B. K.; Kuo, J. L.; Huang, C. C.; Hewak, D. W.; *et al.* Spin-Orbit Splitting in Single-Layer MoS₂ Revealed by Triply Resonant Raman Scattering. *Phys. Rev. Lett.* **2013**, *111*, 126801.
- Berkdemir, A.; Gutierrez, H. R.; Botello-Mendez, A. R.; Perea-Lopez, N.; Elias, A. L.; Chia, C. I.; Wang, B.; Crespi, V. H.; Lopez-Urias, F.; Charlier, J. C.; *et al.* Identification of Individual and Few Layers of WS₂ Using Raman Spectroscopy. *Sci. Rep.* **2013**, *3*, 1755.
- Kang, J.; Tongay, S.; Zhou, J.; Li, J. B.; Wu, J. Q. Band Offsets and Heterostructures of Two-Dimensional Semiconductors. *Appl. Phys. Lett.* **2013**, *102*, 012111.
- Gong, C.; Zhang, H. J.; Wang, W. H.; Colombo, L.; Wallace, R. M.; Cho, K. J. Band Alignment of Two-Dimensional Transition Metal Dichalcogenides: Application in Tunnel Field Effect Transistors. *Appl. Phys. Lett.* **2013**, *103*, 053513.
- Britnell, L.; Ribeiro, R. M.; Eckmann, A.; Jalil, R.; Belle, B. D.; Mishchenko, A.; Kim, Y. J.; Gorbachev, R. V.; Georgiou, T.; Morozov, S. V.; *et al.* Strong Light-Matter Interactions in Heterostructures of Atomically Thin Films. *Science* **2013**, *340*, 1311–1314.
- Bernardi, M.; Palummo, M.; Grossman, J. C. Extraordinary Sunlight Absorption and One Nanometer Thick Photovoltaics Using Two-Dimensional Monolayer Materials. *Nano Lett.* **2013**, *13*, 3664–3670.
- Kang, J.; Tongay, S.; Li, J. B.; Wu, J. Q. Monolayer Semiconducting Transition Metal Dichalcogenide Alloys: Stability and Band Bowing. *J. Appl. Phys.* **2013**, *113*, 143703.
- Komsa, H. P.; Krasheninnikov, A. V. Two-Dimensional Transition Metal Dichalcogenide Alloys: Stability and Electronic Properties. *J. Phys. Chem. Lett.* **2012**, *3*, 3652–3656.
- Xi, J. Y.; Zhao, T. Q.; Wang, D.; Shuai, Z. G. Tunable Electronic Properties of Two-Dimensional Transition Metal Dichalcogenide Alloys: A First-Principles Prediction. *J. Phys. Chem. Lett.* **2014**, *5*, 285–291.
- Conley, H. J.; Wang, B.; Ziegler, J. I.; Haglund, R. F.; Pantelides, S. T.; Bolotin, K. I. Bandgap Engineering of Strained Monolayer and Bilayer MoS₂. *Nano Lett.* **2013**, *13*, 3626–3630.
- Terrones, H.; Lopez-Urias, F.; Terrones, M. Novel Hetero-Layered Materials with Tunable Direct Band Gaps by Sandwiching Different Metal Disulfides and Diselenides. *Sci. Rep.* **2013**, *3*, 1549.
- Li, H.; Zhang, Q.; Yap, C. C. R.; Tay, B. K.; Edwin, T. H. T.; Olivier, A.; Baillargeat, D. From Bulk to Monolayer MoS₂: Evolution of Raman Scattering. *Adv. Funct. Mater.* **2012**, *22*, 1385–1390.
- Lee, C.; Yan, H.; Brus, L. E.; Heinz, T. F.; Hone, J.; Ryu, S. Anomalous Lattice Vibrations of Single- and Few-Layer MoS₂. *ACS Nano* **2010**, *4*, 2695–2700.
- Mao, N. N.; Chen, Y. F.; Liu, D. M.; Zhang, J.; Xie, L. M. Solvatochromic Effect on the Photoluminescence of MoS₂ Monolayers. *Small* **2013**, *9*, 1312–1315.
- Ni, Z. H.; Wang, Y. Y.; Yu, T.; Shen, Z. X. Raman Spectroscopy and Imaging of Graphene. *Nano Res.* **2008**, *1*, 273–291.
- Li, S. L.; Miyazaki, H.; Song, H.; Kuramochi, H.; Nakaharai, S.; Tsukagoshi, K. Quantitative Raman Spectrum and Reliable Thickness Identification for Atomic Layers on Insulating Substrates. *ACS Nano* **2012**, *6*, 7381–7388.
- Li, H.; Wu, J. M. T.; Huang, X.; Lu, G.; Yang, J.; Lu, X.; Zhang, Q. H.; Zhang, H. Rapid and Reliable Thickness Identification of Two-Dimensional Nanosheets Using Optical Microscopy. *ACS Nano* **2013**, *7*, 10344–10353.
- Benamur, M. M.; Radisavljevic, B.; Heron, J. S.; Sahoo, S.; Berger, H.; Kis, A. Visibility of Dichalcogenide Nanolayers. *Nanotechnology* **2011**, *22*, 125706.
- Gutierrez, H. R.; Perea-Lopez, N.; Elias, A. L.; Berkdemir, A.; Wang, B.; Lv, R.; Lopez-Urias, F.; Crespi, V. H.; Terrones, M. Extraordinary Room-Temperature Photoluminescence in Triangular WS₂ Monolayers. *Nano Lett.* **2013**, *13*, 3447–3454.

23. Zhao, W. J.; Ribeiro, R. M.; Toh, M. L.; Carvalho, A.; Kloc, C.; Neto, A. H. C.; Eda, G. Origin of Indirect Optical Transitions in Few-Layer MoS_2 , WS_2 , and WSe_2 . *Nano Lett.* **2013**, *13*, 5627–5634.
24. Zhang, X.; Han, W. P.; Wu, J. B.; Milana, S.; Lu, Y.; Li, Q. Q.; Ferrari, A. C.; Tan, P. H. Raman Spectroscopy of Shear and Layer Breathing Modes in Multilayer MoS_2 . *Phys. Rev. B* **2013**, *87*, 115413.
25. Zhao, Y. Y.; Luo, X.; Li, H.; Zhang, J.; Araujo, P. T.; Gan, C. K.; Wu, J.; Zhang, H.; Quek, S. Y.; Dresselhaus, M. S.; *et al.* Inter Layer Breathing and Shear Modes in Few-Trilayer MoS_2 and WSe_2 . *Nano Lett.* **2013**, *13*, 1007–1015.
26. Chen, Y. F.; Xi, J. Y.; Dumcenco, D. O.; Liu, Z.; Suenaga, K.; Wang, D.; Shuai, Z. G.; Huang, Y. S.; Xie, L. M. Tunable Band Gap Photoluminescence from Atomically Thin Transition-Metal Dichalcogenide Alloys. *ACS Nano* **2013**, *7*, 4610–4616.
27. Tongay, S.; Narang, D. S.; Kang, J.; Fan, W.; Ko, C. H.; Luce, A. V.; Wang, K. X.; Suh, J.; Patel, K. D.; Pathak, V. M.; *et al.* Two-Dimensional Semiconductor Alloys: Monolayer $\text{Mo}_{1-x}\text{W}_x\text{Se}_2$. *Appl. Phys. Lett.* **2014**, *104*, 012101.
28. Tonndorf, P.; Schmidt, R.; Bottger, P.; Zhang, X.; Borner, J.; Liebig, A.; Albrecht, M.; Kloc, C.; Gordan, O.; Zahn, D. R. T.; *et al.* Photoluminescence Emission and Raman Response of Monolayer MoS_2 , MoSe_2 , and WSe_2 . *Opt. Express* **2013**, *21*, 4908–4916.
29. Zeng, H. L.; Liu, G. B.; Dai, J. F.; Yan, Y. J.; Zhu, B. R.; He, R. C.; Xie, L.; Xu, S. J.; Chen, X. H.; Yao, W.; *et al.* Optical Signature of Symmetry Variations and Spin-Valley Coupling in Atomically Thin Tungsten Dichalcogenides. *Sci. Rep.* **2013**, *3*, 1608.
30. Sugai, S.; Ueda, T. High-Pressure Raman-Spectroscopy in the Layered Materials 2h- MoS_2 , 2h- MoSe_2 , and 2h- MoTe_2 . *Phys. Rev. B* **1982**, *26*, 6554–6558.
31. Larentis, S.; Fallahazad, B.; Tutuc, E. Field-Effect Transistors and Intrinsic Mobility in Ultra-Thin MoSe_2 Layers. *Appl. Phys. Lett.* **2012**, *101*, 223104.
32. Sahin, H.; Tongay, S.; Horzum, S.; Fan, W.; Zhou, J.; Li, J.; Wu, J.; Peeters, F. M. Anomalous Raman Spectra and Thickness-Dependent Electronic Properties of WSe_2 . *Phys. Rev. B* **2013**, *87*, 165409.
33. Mead, D. G.; Irwin, J. C. Long Wavelength Optic Phonons in WSe_2 . *Can. J. Phys.* **1977**, *55*, 379–382.
34. Wang, H. T.; Kong, D. S.; Johanes, P.; Cha, J. J.; Zheng, G. Y.; Yan, K.; Liu, N. A.; Cui, Y. MoSe_2 and WSe_2 Nanofilms with Vertically Aligned Molecular Layers on Curved and Rough Surfaces. *Nano Lett.* **2013**, *13*, 3426–3433.
35. Luo, X.; Zhao, Y. Y.; Zhang, J.; Toh, M. L.; Kloc, C.; Xiong, Q. H.; Quek, S. Y. Effects of Lower Symmetry and Dimensionality on Raman Spectra in Two-Dimensional WSe_2 . *Phys. Rev. B* **2013**, *88*, 195313.
36. Terrones, H.; Corro, E. D.; Feng, S.; Poumirol, J. M.; Rhodes, D.; Smirnov, D.; Pradhan, N. R.; Lin, Z.; Nguyen, M. A. T.; Elías, A. L.; *et al.* New First Order Raman-Active Modes in Few Layered Transition Metal Dichalcogenides. *Sci. Rep.* **2014**, *4*, 4215.
37. Lui, C. H.; Malard, L. M.; Kim, S.; Lantz, G.; Laverge, F. E.; Saito, R.; Heinz, T. F. Observation of Layer-Breathing Mode Vibrations in Few-Layer Graphene through Combination Raman Scattering. *Nano Lett.* **2012**, *12*, 5539–5544.
38. Wu, J. X.; Xu, H.; Mu, W. H.; Xie, L. M.; Ling, X.; Kong, J.; Dresselhaus, M. S.; Zhang, J. Observation of Low-Frequency Combination and Overtone Raman Modes in Misoriented Graphene. *J. Phys. Chem. C* **2014**, *118*, 3636–3643.
39. Loudon, R. The Raman Effect in Crystals. *Adv. Phys.* **2001**, *50*, 813–864.
40. Bhagavantam, S.; Venkatarayudu, T. Raman Effect in Relation to Crystal Structure. *Proc. R. Soc. A* **1931**, *130*, 224–258.
41. Chen, Y. F.; Dumcenco, D. O.; Zhu, Y. M.; Zhang, X.; Mao, N. N.; Feng, Q. L.; Zhang, M.; Zhang, J.; Tan, P. H.; Huang, Y. S.; *et al.* Composition-Dependent Raman Modes of $\text{Mo}_{1-x}\text{W}_x\text{S}_2$ Monolayer Alloys. *Nanoscale* **2014**, *4*, 2833–2839.
42. Dumcenco, D. O.; Chen, K. Y.; Wang, Y. P.; Huang, Y. S.; Tiong, K. K. Raman Study of 2h- $\text{Mo}_{1-x}\text{W}_x\text{S}_2$ Layered Mixed Crystals. *J. Alloy. Compd.* **2010**, *506*, 940–943.
43. Xu, H.; Wu, J. X.; Chen, Y. B.; Zhang, H. L.; Zhang, J. Substrate Engineering by Hexagonal Boron Nitride/ SiO_2 for Hysteresis-Free Graphene FETs and Large-Scale Graphene P-N Junctions. *Chem.—Asian J.* **2013**, *8*, 2446–2452.
44. Feng, Q. L.; Zhu, Y. M.; Hong, J. H.; Zhang, M.; Duan, W. J.; Mao, N. N.; Wu, J. X.; Xu, H.; Dong, F. L.; Lin, F.; *et al.* Growth of Large-Area 2D $\text{MoS}_{2(1-x)}\text{Se}_{2x}$ Semiconductor Alloys. *Adv. Mater.* **2014**, *26*, 2648–2653.